

# Letters

## Multifrequency Contrast Source Inversion-Based Permittivity Estimation for Terahertz Multilayer Analysis

Jun Okada and Shouhei Kidera , Senior Member, IEEE

**Abstract**—In this study, the method of estimating permittivity using inverse scattering is presented for multilayered analysis in the terahertz (THz) frequency band. While many studies have been conducted to determine the relative permittivity estimation of multilayer media, most of the studies are based on the time-of-flight (TOF) analysis, which requires the careful consideration of multiple reflection factors and a sufficiently short pulse, i.e., a wider frequency bandwidth, to discriminate the number of TOF from each layer. Therefore, the contrast source inversion-based permittivity estimator exploiting multiple frequency cost function analysis has been introduced. The efficiency of our proposed approach is shown using THz time-domain spectroscopy measurements on two thin layer objects.

**Index Terms**—Contrast source inversion (CSI), multilayer structure analysis, permittivity estimation, terahertz (THz) time domain spectroscopy, terahertz wave.

### I. INTRODUCTION

THERE is an increasing demand for terahertz (THz) wave imaging techniques, which have the potential for various applications, such as the nondestructive or subsurface evaluation of materials [1], medical diagnosis for skin diseases [2], [3], and chemical compound analysis [4] for security screening. In particular, THz time-domain spectroscopy (THz-TDS) generates 3-D profiles of reflection or transmissive coefficients, which can also be used for object identification [5]. In addition, the extraction of complex permittivity is an interesting topic for determining its electrical characteristics. Many studies have been conducted to estimate the permittivity using time-of-flight (TOF) data, assuming a multilayer model in which either the permittivity or the thickness of each layer can be reconstructed [6]. However, the abovementioned TOF-based analysis assumes the use of transmissive responses penetrating into an object, which is not available in most NDT or subsurface imaging scenarios. Some research works on multilayered analysis based on radar

responses exist, such as [7]. While these studies extract the dielectric semblance property of multilayered objects, the abovementioned radar-based approach should transform the reflection responses or TOFs to the dielectric property by compensating for specific physical factors, such as antenna gain, transmitting power, or absorption property of each layer. In addition, focusing on the reflection TOFs-based permittivity estimation, it is necessary to separate the TOFs caused by multiple reflections, requiring a wider frequency bandwidth.

To overcome the abovementioned difficulty, this study introduces an inverse scattering analysis-based permittivity estimation scheme. The problem of retrieving complex permittivity profiles from scattered electric fields measured at a nearby sensor is formulated as a domain integral equation derived from the Maxwell equation. This inverse problem is known as a nonlinear problem with an ill-posed feature, implying that the quantity of data is considerably less than the number of unknowns. Thus, many approaches, such as Born approximation [8] or contrast source inversion (CSI) [9], have been developed. It is well known that the CSI method produces an accurate dielectric profile with much lower complexity than other methods by avoiding the iterative calculation required by forward solvers, i.e., the finite-difference time-domain (FDTD) method. However, the reconstruction accuracy of the CSI is considerably dependent on the balance between measurement data and unknown samples or on the initial estimation of the dielectric constant of each layer.

To address with the abovementioned issue, we introduce homogeneous assumption-based CSI, in which the number of unknowns is considerably reduced to the number of layers due to their homogeneity. The aforementioned single frequency-based method was developed in [10], but it was demonstrated in only ideal numerical situations and was considered a single frequency inversion. Although the results of multifrequency inversion would provide a more reliable estimation, this scheme has not been established. Thus, this study proposes a multifrequency CSI reconstruction scheme that successfully integrates the cost function of each single frequency. Furthermore, as the multiple frequency inversion requires additional computational costs, we combine a sparse sample search with a quadratic function-based interpolation scheme to reduce the total computational cost without losing accuracy. The experimental study shows that our multifrequency extension scheme provides the most accurate

Manuscript received 7 April 2022; revised 20 June 2022; accepted 18 July 2022. Date of publication 25 July 2022; date of current version 3 September 2022. This work was supported by JST FOREST Program, Japan, under Grant JPMJFR2025. (Corresponding author: Shouhei Kidera.)

The authors are with the Graduate School of Informatics and Engineering, University of Electro-Communications, Tokyo 1828585, Japan (e-mail: j.okada358@gmail.com; kidera@uec.ac.jp).

Color versions of one or more figures in this article are available at <https://doi.org/10.1109/TTHZ.2022.3193609>.

Digital Object Identifier 10.1109/TTHZ.2022.3193609

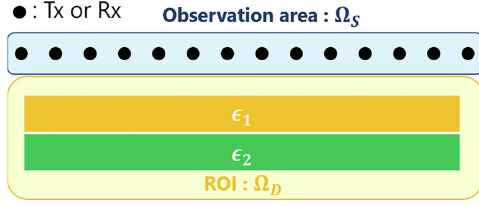


Fig. 1. Observation and object model.

estimation of each relative permittivity when using the two-layer objects composed of polyethylene terephthalate (PET) or polyvinyl chloride (PVC) materials.

## II. METHOD

### A. Observation Model

Observation geometry is shown in Fig 1. A single set of transmitter and receiver is scanned along a straight line whose area is defined as  $\Omega_S$ . The domain including an object is defined as  $\Omega_D$ .  $E^T(\omega; \mathbf{r}_t, \mathbf{r}_r)$  is the total electric field obtained by stimulating a source at  $\mathbf{r}_t$  and recording its scattering signal at  $\mathbf{r}_r$ . A multilayer object has multiple homogeneous layers parallel to the scanning line. The complex-valued scattered signal at the angular frequency  $\omega$  is defined as  $E^S(\omega; \mathbf{r}_t, \mathbf{r}_r) \equiv E^T(\omega; \mathbf{r}_t, \mathbf{r}_r) - E^I(\omega; \mathbf{r}_t, \mathbf{r}_r)$ , where  $E^I(\omega; \mathbf{r}_t, \mathbf{r}_r)$  is the incident electric fields observed in the case with no object. For simplicity, the thickness of each layer is given.

### B. Contrast Source Inversion

The CSI approach is used to determine the relative permittivity of each layer, as proposed in [10]. Here,  $E^S(\omega; \mathbf{r}_t, \mathbf{r}_r)$  is expressed in the domain integral equation

$$E^S(\omega; \mathbf{r}_t, \mathbf{r}_r) = (k^B)^2 \int_D G^B(\omega; \mathbf{r}_r, \mathbf{r}) w(\omega; \mathbf{r}_t, \mathbf{r}) d\mathbf{r} \quad (1)$$

where  $k^B$  is the wavenumber of the background media and  $G^B(\omega; \mathbf{r}_r, \mathbf{r})$  is Green's function of the background media.  $w(\omega; \mathbf{r}_t, \mathbf{r}) \equiv E^T(\omega; \mathbf{r}_t, \mathbf{r}_r) \chi(\omega; \mathbf{r})$  is called the contrast source and is defined by  $\chi(\omega; \mathbf{r}) \equiv \epsilon(\omega; \mathbf{r}) / \epsilon^B(\omega; \mathbf{r}) - 1$ , where  $\epsilon(\omega; \mathbf{r})$  and  $\epsilon^B(\omega; \mathbf{r})$  are the complex permittivities with and without an object at the angular frequency  $\omega$ , respectively. The CSI takes advantage that (1) would be satisfied not only at  $\Omega_S$  but also at  $\Omega_D$ . Thereafter, the two physical conditions outlined previously are used for the following cost function:

$$F(\chi, w, \omega) \equiv \frac{\sum_{\mathbf{r}_t} \|E^S(\omega; \mathbf{r}_t, \mathbf{r}_r) - \mathcal{G}^S[w]\|_{\Omega_S}^2}{\sum_{\mathbf{r}_t} \|E^S(\omega; \mathbf{r}_t, \mathbf{r}_r)\|_{\Omega_S}^2} + \frac{\sum_{\mathbf{r}_t} \|\chi(\mathbf{r}) E^I(\omega; \mathbf{r}_t, \mathbf{r}') - w(\omega; \mathbf{r}_t, \mathbf{r}) + \chi(\mathbf{r}) \mathcal{G}^D[w]\|_{\Omega_D}^2}{\sum_{\mathbf{r}_t} \|\chi(\omega; \mathbf{r}) E^I(\omega; \mathbf{r}_t, \mathbf{r}')\|_{\Omega_D}^2} \quad (2)$$

Notably, the input data as  $E^S(\omega; \mathbf{r}_t, \mathbf{r}_r)$  is a complex value, and both magnitude and phase of these data are used for the inversion.

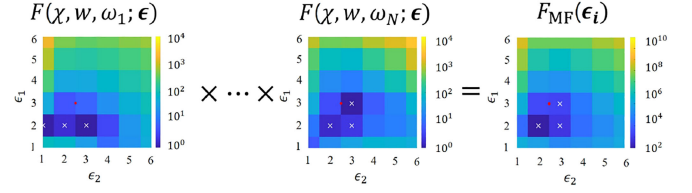


Fig. 2. Proposed scheme for multiple frequency integration of the CSI cost functions.

Here, the following notations are defined as:

$$\mathcal{G}^S[w] = (k^B)^2 \int_{\Omega_D} G^B(\omega; \mathbf{r}_r, \mathbf{r}) w(\omega; \mathbf{r}_t, \mathbf{r}) d\mathbf{r}, (\mathbf{r} \in \Omega_S) \quad (3)$$

$$\mathcal{G}^D[w] = (k^B)^2 \int_{\Omega_D} G^B(\omega; \mathbf{r}', \mathbf{r}) w(\omega; \mathbf{r}_t, \mathbf{r}) d\mathbf{r}, (\mathbf{r}' \in \Omega_D) \quad (4)$$

where  $\|\cdot\|_{\Omega_S}^2$  and  $\|\cdot\|_{\Omega_D}^2$  are the  $l_2$  norms determined in the  $\Omega_S$  and  $\Omega_D$  areas, respectively.  $E^T(\omega; \mathbf{r}_t, \mathbf{r}_r)$  and  $\chi(\omega; \mathbf{r})$  are sequentially optimized by minimizing the cost function defined in (2). As a notable feature of the CSI, it is capable of optimizing not only the object function  $\chi$  but also  $E^T$  via the contrast source variable  $w$ , thus avoiding the computationally expensive forward solver. The optimization algorithm of (2) has been attributed in detail, for example, in [9], where the conjugate gradient iterative method was used.

The literature [10] achieves an accurate permittivity estimation for multilayered object, by minimizing the abovementioned cost function for each combination of the relative permittivity defined as  $\epsilon \equiv (\epsilon_1, \dots, \epsilon_M)$ . However, it assumes single frequency inversion, which is more sensitive to random noises or other error factors caused by data calibration, especially when real data are used.

### C. Multifrequency Extension

Thus, this study introduces multifrequency extension of the method [10] as follows. Assuming a nondispersive media, a number of cost functions in each frequency are integrated in a product form as

$$F_{MF}(\epsilon) = \prod_j^N \min_w F(\chi, w, \omega_j; \epsilon). \quad (5)$$

Only the variable  $w$  is updated when minimizing each cost function  $F(\chi, w, \omega_j; \epsilon)$ , where the  $\chi$  is fixed as the profile generated by homogeneous multilayered media with the given permittivity  $\epsilon$ . Note that, a product form in (5) can maintain the impact with much a smaller residual of  $F(\chi, w, \omega_j, \epsilon)$ , which would be possibly neglected in a simple summation form. Thereafter, the optimized combination of relative permittivity  $\hat{\epsilon}$  is determined as

$$\hat{\epsilon} = \arg \min_{\epsilon} F_{MF}(\epsilon). \quad (6)$$

Fig. 2 shows the schematic illustration of the proposed method.

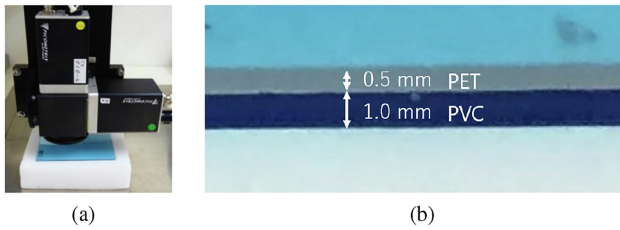


Fig. 3. Experimental setup using THz-TDS and double layered objects. (a) THz-TDS. (b) PET + PVC.

### III. RESULTS

#### A. Experimental Setup

The experimental setup is shown in Fig. 3 using the THz-TDS system supplied by Spectra Design Co., Ltd., Japan, in which a photoconductive antenna with a focal length of 25 mm is scanned along the  $x$ -axis with a 0.25-mm spacing. The scanning range is 40 mm, and there are 320 samples. Here, the 10 times coherent averaging is used and the measurement time for each sampled point is 0.01 s. We assume the two types of targets composed of PET (0.5 mm thick sheet) and PVC (1.0 mm thick sheet). Because this scenario implies a relatively narrow and lower band from 100 to 200 GHz, and the relative permittivity of PET and PVC is almost constant over these frequency bands, [13], [14], the nondispersive assumption of the proposed method might be applied in this case. When setting the two-layer objects, the upper and lower layers are set to PET and PVC, respectively, as shown in Fig. 3. The transmissive responses of each PET and PVC sheet are analyzed to get the referential values of the relative permittivities of 2.96 and 2.66, respectively.

We performed a simple data calibration process as follows. First, the reflection responses of each PET or PVC single layer are measured and simultaneously generated these reflections using the FDTD numerical solver, thereby assuming the same observation model. Let  $E_{\text{sim}}^T(\omega)$  and  $E_{\text{sim}}^I(\omega)$  be the total and incident electric fields generated by the FDTD method at the given transmitter and receiver pair, in assuming a calibration object, such as PET or PVC with a known complex permittivity. In addition,  $S_{\text{exp}}^T(\omega)$  and  $S_{\text{exp}}^I(\omega)$  are the  $S_{21}$  parameters in the experiment with and without calibration objects, respectively. A compensation coefficient  $\zeta(\omega)$  is introduced as follows:

$$\zeta(\omega) \equiv \frac{E_{\text{sim}}^T(\omega) - E_{\text{sim}}^I(\omega)}{S_{\text{exp}}^T(\omega) - S_{\text{exp}}^I(\omega)}. \quad (7)$$

Let  $S_{\text{exp}}^S(\omega) \equiv S_{\text{exp}}^T(\omega) - S_{\text{exp}}^I(\omega)$  be the scattered field produced by an unknown object, and it is transformed into simulation data as  $E_{\text{exp}}^S(\omega) = \zeta(\omega) S_{\text{exp}}^S(\omega)$ . Subsequently, using the linear transfer function model, the measured data could be transformed into simulation data, and the aforementioned approach is frequently utilized as a calibration technique [11], [12]. Notably, as long as the consistency between numerical and actual models is maintained, the foregoing calibration is applicable to not only transmission but also reflection data. The cell size is 20  $\mu\text{m}$  in both the FDTD and CSI models.

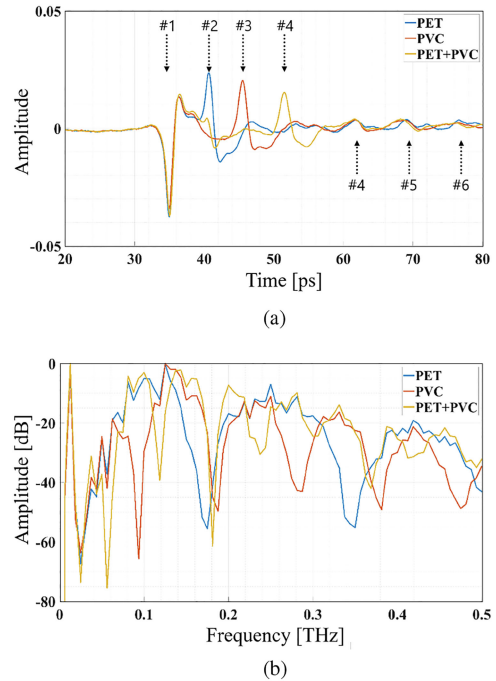


Fig. 4. Experimental data in the time and frequency domains. (a) Time. (b) Frequency.

#### B. Permittivity Estimation

The reflection responses of each case in the frequency and time domain are shown in Fig. 4. Focusing on the reflections from the two layers of PET and PVC, we could identify two local peaks (#2 and #4) in the time-domain responses after the surface reflections (#1), which are regarded as the reflections from the bottom layers of PET and PVC. Note that the #2 local peak in the “PET + PVC” case is less than that in the “PET only” case because the dielectric constant between PET and PVC is lower than that between PET and air. Thereafter, the local peak #2 for the “PET + PVC” case might be masked by the first surface reflection responses (#1). Furthermore, because there are several multiple reflections in the later responses from 60 ps (e.g., #4, #5, and #6), the TOF-based permittivity estimation is hardly applicable because it should recognize the order of the multiple reflections. Furthermore, there are substantial responses beneath 25 GHz, which are false responses owing to the DC offset effect and should not be used for the inversion scheme. Note that each frequency response in Fig. 4 is dominant from 50 to 300 GHz, which is in the lower THz band. However, there are certain advantages to adopting this band, such as deeper penetration depth and less absorption by the material. Furthermore, because the scattered data should be generated by the FDTD method, the lower frequency band has a benefit for lower complexity in the calibration process because the FDTD requires the condition that its cell size should be less than 1/10 wavelength, and the total number of cells would be lowered in assuming lower frequency band at the same scale of the object. The distribution of the minimized cost function of the CSI for each permittivity combination, which is defined in (2), is shown in Fig. 5 for both single and multiple frequencies. There are significant variations

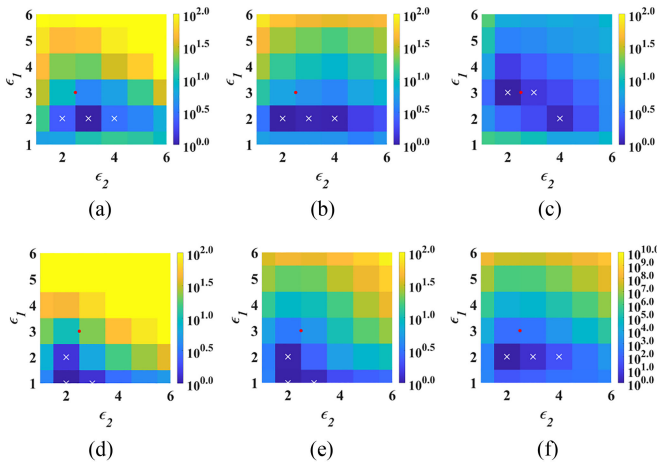


Fig. 5. Residual of cost function in the CSI for each combination of  $(\epsilon_1, \epsilon_2)$ . Red solid circles and white X denote the original and optimized combination of  $(\epsilon_1, \epsilon_2)$ , respectively. Color denotes the cost function of the CSI as  $F(\chi, w)$  in log scale. (a)  $f = 0.05$  THz. (b)  $f = 0.75$  THz. (c)  $f = 0.10$  THz. (d)  $f = 0.13$  THz. (e)  $f = 0.15$  THz. (f) Multifrequency.

TABLE I  
ESTIMATIONS OF RELATIVE PERMITTIVITY WITH EACH SINGLE AND MULTIPLE FREQUENCIES

	$(\epsilon_1, \epsilon_2)$	Errors
Reference	(2.96,2.66)	
Single Freq. @ 0.050 THz	(1.80,3.56)	(-1.16,0.90)
Single Freq. @ 0.075 THz	(1.67,3.53)	(-1.29,0.87)
Single Freq. @ 0.100 THz	(3.46,3.93)	(0.5,1.27)
Single Freq. @ 0.131 THz	(1.19,3.40)	(-1.77,0.74)
Single Freq. @ 0.150 THz	(1.21,3.36)	(-1.75, 0.7)
Multi Freq. (Proposed)	(2.69,3.25)	(-0.27,0.59)

in the frequencies of minimals, as shown in Figs. 5(a)–(e), which are caused by noise or other calibration errors. Conversely, the proposed scheme, namely, multifrequency integration [see Fig. 5(f)], can provide an appropriate optimization point. The estimated permittivities are summarized in Table I. Note that the sparsely sampled profiles in Fig. 5 are interpolated using a quadratic interpolation scheme, which remarkably reduces the total computational time. The proposed scheme provides the most accurate estimate of the relative permittivity of both PET and PVC layers when compared with the single frequency scheme, as given in Table I.

### C. Discussions

The following are explanations of the merits and limits of this strategy. First, the computational cost would be crucial in the case of more numbers of layers because the proposed method is based on a total search for all combinations of relative permittivity of each layer. The complexity would rise to the order of  $O(M^N)$ , where  $N$  denotes the number of layers,  $M$  denotes the sampling numbers for each layer, and  $O(*)$  denotes the Landau notation. In such cases, we require an efficient optimization algorithm for multidimensional nonlinear optimization, such as particle swarm optimization or genetic algorithm, or must

make available an appropriate initial estimate when using a local optimization algorithm, such as conjugate gradient optimizer.

Second, in regard with applicable thickness of layer, there are some advantages or disadvantages to the radar-based approaches, such as [7]. In terms of applicable minimum thickness, the proposed CSI approach is not significantly limited, unlike the radar approach, because our approach does not need to decompose the radar responses to acquire high-resolution TOF profiles, which are available over large frequency bands. Because we are considering the  $20 \mu\text{m}$  cell size in this case, the minimum thickness, in this case, is the same as the estimated cell size. Furthermore, assuming a thin layer, the number of unknowns for the total fields could be considerably reduced, which brings us a positive effect to solve the inverse scattering issue, by alleviating ill-posed conditions. Conversely, while dealing with a thicker layer, we must calculate the total fields of the larger area layer to calculate the cost function of the CSI, which considerably increases the complexity. However,  $\chi$ , namely, the dielectric profile is fixed in the CSI optimization sequence, and only the contrast source  $w$  (namely the total field) is an optimization variable. In general, the distribution of the total fields have not so much higher spatial frequency compared with the center wavelength in the assumed media, we could apply some undersampling technique in dealing with a larger area, where the Nyquist criteria should be satisfied. Nonetheless, in much thicker cases, the radar-based approach is expected to outperform the proposed method, particularly in terms of computational costs.

Third, because we assumed that each layer has a dielectric property that is frequency independent, the proposed method would be inaccurate for a dispersive medium. However, the CSI could be applicable to single or narrower frequency responses, and then, if some appropriate frequency-dependent model, such as Debye and Cole–Cole, would be applicable, this scheme could be extended to the dispersive model, where several permittivities obtained from single or narrower responses are fitted to the aforementioned frequency-dependent model.

Finally, if the nondispersive feature is maintained across the tested frequency range, it is expected that the reconstruction accuracy of the proposed method would be improved by using a larger number of frequency points, as in the approach [15]. However, the proposed method optimizes the cost function at each frequency in (2), where sufficient repetitions are necessary to minimize a cost function. The computational costs become more critical using more number of frequency points. Owing to the limitations stated previously, we choose five different frequency points in this situation.

## IV. CONCLUSION

This study presented the multifrequency integrated permittivity estimation scheme for THz multilayer object analysis using the CSI cost function from only reflection responses. The minimization results for each frequency are integrated into a product function, allowing us to determine an appropriate solution from multiple minimization results. The experiments conducted using the THz-TDS measurement system demonstrated that our

proposed method provided more accurate permittivity estimations for both layers. As our method is based on a reflection measurement system, it is more widely applicable to various applications, such as nondestructive subsurface diagnosis or medical diagnosis compared with the transmissive observation model. Note that each thickness of the layer is given in this case. However, there are existing studies to simultaneously optimize the thickness and dielectric constant of each layer using the CSI scheme, such as [10], and then, it is our future work to combine such approach into the proposed method.

## REFERENCES

- [1] R. Fukusawa, "Terahertz imaging: Widespread industrial application in non-destructive inspection and chemical analysis," *IEEE Trans. THz Sci. Technol.*, vol. 7, no. 3, pp. 1121–1127, Nov. 2015.
- [2] H. Liu et al., "Dimensionality reduction for identification of hepatic tumor samples based on terahertz time-domain spectroscopy," *IEEE Trans. THz Sci. Technol.*, vol. 8, no. 3, pp. 271–277, May 2018.
- [3] K. I. Zaytsev et al., "Highly accurate *in vivo* terahertz spectroscopy of healthy skin: Variation of refractive index and absorption coefficient along the human body," *IEEE Trans. THz Sci. Technol.*, vol. 5, no. 5, pp. 817–827, Sep. 2015.
- [4] K. W. Kim, H. Kim, J. Park, J. K. Han, and J. Son, "Terahertz tomographic imaging of transdermal drug delivery," *IEEE Trans. THz Sci. Technol.*, vol. 2, no. 1, pp. 99–106, Jan. 2012.
- [5] D. M. Hailu, A. K. Ayesheshim, and D. Saeedkia, "Multi-layer plastic bottle and preform thickness measurement using terahertz pulses," in *Proc. Photon. North*, 2016, pp. 1–4.
- [6] S. Krimi, J. Jonuscheit, G. Von Freymann, R. Urbansky, and R. Beigang, "Highly accurate thickness measurement of multi-layered automotive paints using terahertz technology," *IEEE Trans. Geosci. Remote Sens.*, vol. 48, no. 4, pp. 1993–2004, Apr. 2010.
- [7] N. S. Schreiner, W. Sauer-Greff, R. Urbansky, G. von Freymann, and F. Friederich, "Multilayer thickness measurements below the Rayleigh limit using FMCW millimeter and terahertz waves," *Sensors*, vol. 19, no. 18, 2019, Art. no. 3910.
- [8] W. C. Chew and Y. M. Wang, "Reconstruction of two-dimensional permittivity distribution using the distorted born iterative method," *IEEE Trans. Med. Imag.*, vol. 9, no. 2, pp. 218–225, Jun. 1990.
- [9] P. M. van den Berg and A. Abubakar, "Contrast source inversion method: State of art," *Prog. Electromagn. Res.*, vol. 34, pp. 189–218, 2001.
- [10] H. Morimoto, Y. Yamauchi, and S. Kidera, "Contrast source inversion-based multilayered object analysis for terahertz wave imaging," *IEEE Geosci. Remote Sens. Lett.*, vol. 19, 2022, Art. no. 8018005.
- [11] M. Ostadrahimi et al., "Analysis of incident field modeling and incident/scattered field calibration techniques in microwave tomography," *IEEE Antennas Wireless Propag. Lett.*, vol. 10, pp. 900–903, 2011.
- [12] T. Hanabusa, T. Morooka, and S. Kidera, "Deep-learning-based calibration in contrast source inversion based microwave subsurface imaging," *IEEE Geosci. Remote Sens. Lett.*, vol. 19, 2022, Art. no. 3006805.
- [13] N. Nagai and R. Fukusawa, "Abnormal dispersion of polymer films in the THz frequency region," *Chem. Phys. Lett.*, vol. 388, no. 4–6, pp. 479–482, 2004.
- [14] Y. S. Jin, G. J. Kim, and S. G. Jeon, "Terahertz dielectric properties of polymers," *J. Korean Phys. Soc.*, vol. 49, no. 2, pp. 513–517, Aug. 2006.
- [15] Tamminen, "Extraction of thickness and water-content gradients in hydrogel-based water-backed corneal phantoms via submillimeter-wave reflectometry," *IEEE Trans. THz Sci. Technol.*, vol. 11, no. 6, pp. 647–659, Nov. 2021.